CMOS Compatible Reconfigurable Silicon Photonic Lattice Filters Using Cascaded Unit Cells for RF-Photonic Processing

Binbin Guan, Stevan S. Djordjevic, *Student Member, IEEE*, Nicolas K. Fontaine, *Member, IEEE*, Linjie Zhou, Salah Ibrahim, Ryan P. Scott, *Member, IEEE*, David J. Geisler, *Member, IEEE*, Zhi Ding, *Fellow, IEEE*, and S. J. Ben Yoo, *Fellow, IEEE*

(Invited Paper)

***Abstract*—This paper presents an overview of a complementary metal–oxide–semiconductor-compatible, programmable, analog optical lattice filter based on silicon unit cells arrayed in large-scale photonic integrated circuits. The unit cell employs a combination of a ring resonator and a Mach–Zehnder interferometer with tunable phase elements in both of the paths. Each proposed unit cell contributes a separately controllable pole and zero pair. Under various configurations, we experimentally achieved >60-dB two-tone spurious-free dynamic range. For more sophisticated signal processing, we experimentally demonstrated an optical lattice filter with four cascaded unit cells capable of dynamically reconfiguring between a bandpass filter and a notch filter. The reconfiguration of the unit-cell and four-cell silicon lattice filter is based on a recursive algorithm, which brings new possibilities to RF photonic processing and a wide range of applications with design scalability to a large number of poles and zeros. The experimental results and the recursive algorithms show potentials for scaling to higher order filter designs.**

***Index Terms*—Complementary metal–oxide–semiconductor (CMOS) process, filtering algorithms, microwave photonics, optical filters, optical modulation, silicon photonics.**

I. Introduction

RF-PHOTONIC processing of microwave signals is of considerable interest for replacing electrical signal processing in many cases, due to possible advantages for higher bandwidth, lower power consumption and low latency [1], [2]. There is an increasing demand of all-optical signal processing approach in a broad range of applications [1], [3]–[6]. To match the requirement of diverse signal processing in electrical systems, all-optical processing components must be easily reconfigurable with full control over a large number of poles and zeros in the transfer function. Among the many RF-photonic processing components that exist, optical lattice filters are a good all-purpose solution due to their ability to generate complicated transfer functions by cascading identical unit cells. State-of-art research into optical reconfigurable filter includes both silicon and InP platforms [7]–[10]. In particular, [7] demonstrates the use of InP based reconfigurable lattice filter with monolithically integrated coupled ring structures, while [8] shows a silicon reconfigurable filter with thermal tuning. In this paper, we discuss a complementary metal–oxide–semiconductor (CMOS) compatible silicon optical lattice filter. We also leverage the high-yield, low-cost and repeatable performance of silicon device fabrication technology. In addition, our optical lattice filter is dynamically reconfigurable using a recursive algorithm to achieve the (nontrivial) desired transfer functions [11]. As a result, the optical lattice filter can benefit a wide range of applications, such as narrow bandwidth filter, correlation, multiplexing distortion compensation [12], etc.

The content of the paper is organized as follows. Section II includes a description of the architecture of the unit-cell and four-cell optical lattice filters with a mathematical description of the transfer function. In Section III, we provide an explanation of the recursive algorithm used for arbitrary transfer function synthesis in unit-cells and a derivation of the four-cell transfer function and recursive algorithm. In Section IV, we discuss the details of silicon lattice filter fabrication. In Section V, we show experimental characterization results of unit-cell and four-cell optical lattice filters. In Section VI, we demonstrate experimental results for unit-cell filter and four-cell transfer function reconfiguration, for both bandpass filters and notch filters. In Section VII, we also discuss potential applications towards RF signal processing using an optical lattice filter. Finally, Section VIII summarizes this work.

Manuscript received October 15, 2013; revised December 16, 2013; accepted December 17, 2013. This work was supported in part by DARPA MTO SiPhASER project Grant no. HR0011-09-1-0013.

B. Guan, S. S. Djordjevic, R. P. Scott, Z. Ding, and S. J. Ben Yoo are with the Department of Electrical and Computer Engineering, University of California, Davis, CA 95616 USA (e-mail: rayguan@ucdavis.edu; sdjordjevic@ucdavis.edu; rpscott@ucdavis.edu; zding@ucdavis.edu; sbyoo@ucdavis.edu).

N. K. Fontaine was with the University of California, Davis, CA 95616 USA. He is now with Alcatel-Lucent Bell Laboratories, Holmdel, NJ 07733 USA (e-mail: nicolas.fontaine@alcatel-lucent.com).

L. Zhou was with the University of California, Davis, CA 95616 USA. He is now with the Department of Electronic Engineering, Shanghai Jiao Tong University, Minhang District, Shanghai, China (e-mail: ljzhou@sjtu.edu.cn).

S. Ibrahim was with the University of California, Davis, CA 95616 USA. He is now with NTT Photonics Laboratories, Atsugi-shi, Kanagawa Pref. 243-0198, Japan (e-mail: ibrahim.salah@lab.ntt.co.jp).

D. J. Geisler was with the University of California, Davis, CA 95616 USA. He is now with the Massachusetts Institute of Technology Lincoln Laboratory, Lexington, MA 02420 USA (e-mail: david.geisler@ll.mit.edu).

Color versions of one or more of the figures in this paper are available online at http://ieeexplore.ieee.org.

Digital Object Identifier 10.1109/JSTQE.2013.2296233

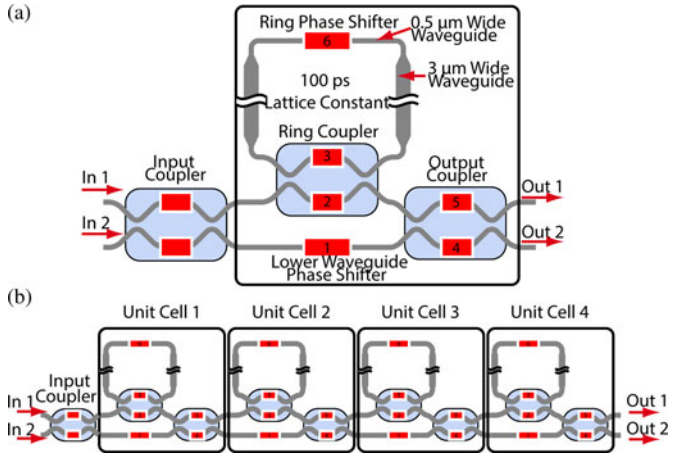

Fig. 1. Schematic design of (a) single unit-cell filter and (b) four-unit-cell filter. [13].

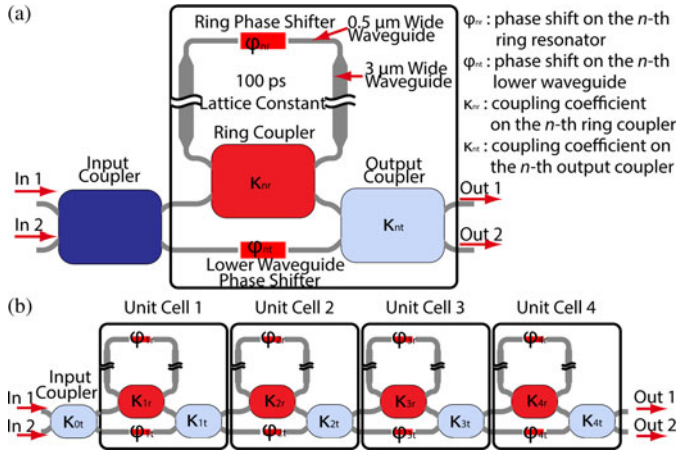

Fig. 2. Definitions for the (a) unit-cell structure and the (b) four-cell structure.

II. Unit-Cell and Four-Cell Cascaded Reconfigurable Lattice Filter

Fig. 1(a) [13] shows the structure of a unit-cell and four-cell silicon optical lattice filter. The structure consists of a 2×2 Mach–Zehnder interferometer (MZI) with a ring resonator on the upper path and a straight waveguide with phase shifter on the lower path. Connecting the two outputs to the two inputs of the following unit cell constructs the lattice filter. In a unit-cell structure, the ring resonator defines the lattice constant [e.g., the temporal spacing of impulses, or the inverse of the free spectrum range (FSR)]. In this case, the lattice constant is 100 ps, corresponding to a 10-GHz FSR. The phase shifter in the resonator and the ring resonator waveguide round trip loss determine the phase and the magnitude of the pole. Tuning the ring coupler phase shifters [labeled as 2 and 3 in Fig. 1(a)] vary the coupling strength between the ring resonator and the straight waveguide in the upper path of the 2×2 MZI. Therefore, the unit-cell structure can produce both finite-impulse response (FIR) and infinite-impulse response (IIR) features. When the coupling strength is weak, the unit-cell filter is primarily IIR with narrow resonance features in the spectrum. Alternatively, when the coupling strength is 100%, the unit-cell becomes a two-tap FIR filter, with a 100-ps delay between the two taps. The zeros of the lattice filter transfer function are dependent on all of the phase shifters of the unit-cell structure.

Phase shifters which are based on free-carrier plasma dispersion effect [14] in silicon photonics, are the basic tuning elements for each unit-cell. We defined lateral p-i-n carrier injection trenches by ion implantation. Required phase shift is induced by injecting current into the resulting p-i-n diode.

Fig. 1(b) shows the four-cell lattice filter which is simply created by cascading four identical unit-cells together. As we discussed above, the lattice filter has the advantage of facilitating the synthesis of high-order transfer functions by tuning each unit-cell.

To analyze the operation of the unit-cell and four-cell filters, we will define Φ_n as the 2×2 transfer matrix for the nth unit-cell structure where Fig. 2(a) and (b) specify the variables associated with the structures that constitute the filter. Here, κ_{nt} is the coupling coefficient of the output coupler, κ_{nr} is the coupling coefficient of the ring coupler, θ_{nt} is the angle description of the coupling coefficient for output coupler, φ_{nr} is the phase of the ring resonator, φ_{nt} is the phase of the lower arm waveguide, and C_{nr} is defined as the coupling coefficient of the of the ring coupler. The 2×2 transfer matrix is then defined as

$$\Phi_n = \begin{bmatrix} c_{nt} & -js_{nt} \\ -js_{nt} & c_{nt} \end{bmatrix} \begin{bmatrix} \frac{-e^{-j\varphi_{nr}} A_n^R(z)}{A_n(z)} & 0 \\ 0 & e^{-j\varphi_{nt}} \end{bmatrix}$$

$$\Phi_0 = \begin{bmatrix} c_{0t} & -js_{0t} \\ -js_{0t} & c_{0t} \end{bmatrix} \text{ for the input coupler} \quad (1)$$

where

$$c_{nt} = \sqrt{1-\kappa_{nt}} = \cos(\theta_{nt})$$
$$s_{nt} = \sqrt{\kappa_{nt}} = \sin(\theta_{nt}) \quad (2)$$

and

$$A_n(z) = 1 - c_{nr} e^{-j\varphi_{nr}} z^{-1}$$
$$A_n^R(z) = -c_{nr} e^{j\varphi_{nr}} + z^{-1} \quad (3)$$

when z^{-1} is defined as $\exp(j\omega\Delta\tau)$ and $\Delta\tau$ is the optical delay per round trip in the ring resonator.

In addition, the input coupler is a 2×2 MZI. The transfer matrix of the input coupler is in (1) as Φ_0. Since the input coupler only affects the zero tuning. Therefore, in our experiment, we usually set the input coupler's coupling coefficient to 50% and used other phase shifters [e.g., phase shifter 1, 4 and 5 labeled in Fig. 1(a)] in the unit-cell structure to adjust the zero.

Filter poles are independently controlled by each unit cell. However, the zeros are coupled together. As a result, it requires a recursive algorithm to fully control the zeros. We will explain the recursive algorithm for filter synthesis in Section III.

III. Reconfigurable Lattice Filter Synthesis

There is only one pole and one zero in the unit-cell transfer function. Therefore, the tuning algorithm is straight forward and mainly consists of characterizing the performance of each phase

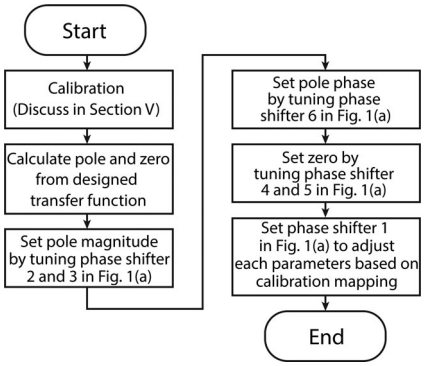

Fig. 3. Unit-cell optical filter reconfiguration flow chart.

shifter and mapping the pole or zero movement as a function of injected current. We will discuss phase shifter characterization in Section V. From (3), for a unit-cell structure, phase of the pole is fully controlled by the phase shifter on the ring resonator [labeled as 6 in Fig. 1(a)], whereas the magnitude of the pole is set by controlling the coupling coefficient to the ring. All of the phase shifters will affect the value of the filter's zero.

Fig. 3 shows the flow chart of the filter synthesis for a unit-cell structure. To start with, we characterize the complex transfer function of the filter with an optical vector network analyzer (OVNA) which is described in detail in Section V. The calibration process is defined as using characterization results to build up the mapping between optical parameters (e.g., κ_{nr}) and the phase shifter's injected current. After calibration, we need to calculate the desired pole and zeros from the transfer function. Then we use phase shifters 2, 3, and 6 to control magnitude and phase of the pole, and use phase shifters on the output coupler [labeled as 4 and 5 in Fig. 1(a)] to control the zero. In the last step of the flow chart, phase shifter 1 in the bottom path of the 2×2 is used for fine tuning all of the parameters.

The reconfiguration algorithm for four-cell filter is more complex and challenging, compared to unit-cell filter tuning. Jinguji *et al*. [11] has previously demonstrated a recursive algorithm for a standard cascaded lattice filter.

The recursion starts with fitting the two port measurement result with an N-pole and N-zero transfer function model. We use normalized energy error (NEE) as the filter fidelity metric [15], which is the ratio between the energy of the error spectrum [i.e., $|T_m(z) - T_f(f)|^2$] and the energy of the fitted spectrum [i.e., $|T_f(z)|^2$)] where $T_m(z)$ and $T_f(z)$ are defined as the measured spectrum and fitted spectrum, respectively. In this case, we have two transfer functions $T_1(z)$ and $T_2(z)$ from the measurement output fitting results. These transfer functions are given by [16]

$$T_1(z) = \frac{H_N(z)}{G_N(z)}, \quad T_2(z) = j\frac{F_N(z)}{G_N(z)} \tag{4}$$

where

$$\begin{aligned} H_N(z) &= h_0^N + h_1^N z^{-1} + h_2^N z^{-2} + \cdots + h_N^N z^{-N} \\ F_N(z) &= f_0^N + f_1^N z^{-1} + f_2^N z^{-2} + \cdots + f_N^N z^{-N} \\ G_N(z) &= g_0^N + g_1^N z^{-1} + g_2^N z^{-2} + \cdots + g_N^N z^{-N}. \end{aligned} \tag{5}$$

The general transfer function of a four-cell cascaded optical lattice filter, $\Phi_N(z)$, is the 2×2 transfer matrix of the Nth order lattice filter and is given by

$$\Phi_{N0} = \prod_{n=0}^{N} \Phi_n = \frac{1}{G_N(z)} \begin{bmatrix} H_N(z) & jF_N^R(z) \\ jF_N(z) & H_N^R(z) \end{bmatrix} \tag{6}$$

where H_N^R and F_N^R are reverse polynomials, and can be easily derived from the inverse of the zeros of H_N and F_N. The only difference is limited in a real constant factor and it can be derived based on consistent power from the first column of the matrix and the second column of the matrix (6). We can rewrite the matrix in (6) with one-step recursion as

$$\begin{aligned} \frac{1}{G_N(z)} \begin{bmatrix} H_N(z) & jF_N^R(z) \\ jF(z) & H_N^R(z) \end{bmatrix} &= \frac{\Phi_N(z)}{G_{N-1}(z)} \\ &\times \begin{bmatrix} H_{N-1}(z) & jF_{N-1}^R(z) \\ jF_{N-1}(z) & H_{N-1}^R(z) \end{bmatrix}. \end{aligned} \tag{7}$$

An inverse matrix calculation of (7) generates H_{N-1}, F_{N-1}, $\theta_{Nt}, \theta_{Nt}, \varphi_{Nt}$ and φ_{Nr} in (8)–(11) below where ρ_N is the root of $A_N(z)$ [16]:

$$\theta_{Nt} = \arctan\left(-\frac{F_N(\rho_N)}{H_N(\rho_N)}\right) \tag{8}$$

$$\theta_{Nt} = \arctan\left(-\frac{F_N(\rho_N)\,\alpha}{H_N(\rho_N)}\right) \text{ for more complete form} \tag{9}$$

$$\begin{aligned} &\arg\left(\frac{H_{N-1}(\rho_N)}{F_{N-1}(\rho_N)}\right) = 0 = \varphi_{Nr} - \varphi_{Nt} \\ &+ \arg\left(\frac{A_N(\rho_{N-1})\left(-c_{Nt}H_N(\rho_{N-1}) + s_{Nt}F_N(\rho_{N-1})\right)}{A_N^R(\rho_{N-1})\left(s_{Nt}H_N(\rho_{N-1}) + c_{Nt}F_N(\rho_{N-1})\right)}\right) \end{aligned} \tag{10}$$

$$\begin{aligned} \varphi_{Nt} &= \varphi_{Nr} + \arg \\ &\times \left(\frac{A_N(\rho_{N-1})\left(-c_{Nt}H_N(\rho_{N-1}) + s_{Nt}F_N(\rho_{N-1})\right)}{A_N^R(\rho_{N-1})\left(s_{Nt}H_N(\rho_{N-1}) + c_{Nt}F_N(\rho_{N-1})\right)}\right). \end{aligned} \tag{11}$$

The one-step recursion reduces the polynomial order by one. We add a constant complex α, to make the content of the expression in (9) a real number. Physically, α arises from magnitude and phase differences between the two outputs of the device that occur when coupling from the waveguide to a fiber, or the fiber length differences of the two outputs. In the end, we need to make sure the ratio of $[H_{N-1}(\rho_{N-1})]/[F_{N-1}(\rho_{N-1})]$ is a real number.

A recursive algorithm is helpful for retrieving the optical parameters, such as coupling coefficients, and phase shifts of each unit-cell. However, we have to build a mapping between zero tuning (e.g., phase shifter tuning) and optical parameter (e.g., phase, coupling coefficients) tuning. We use a modified 2×2 MZI to present this relation. Fig. 4(a) shows the standard structure of a directional coupler and Fig. 4(b) shows the

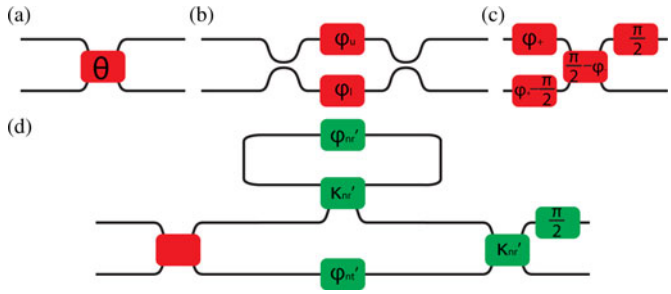

Fig. 4. (a) A standard coupler. (b) A MZI coupler with two phase shifters on both arms. (c) Modified MZI coupler. (d) Modified unit-cell structure.

structure of an MZI coupler. The 2×2 matrix of a directional coupler is given by

$$\begin{bmatrix} A_n \\ B_n \end{bmatrix} = \begin{bmatrix} \cos\theta & -j\sin\theta \\ -j\sin\theta & \cos\theta \end{bmatrix} \begin{bmatrix} A_{n-1} \\ B_{n-1} \end{bmatrix}. \tag{12}$$

We can modify the MZI coupler as a directional coupler, with extra phase shift on both inputs and outputs [Fig. 4(c)]. This transformation is

$$\begin{aligned} \begin{bmatrix} A_n \\ B_n \end{bmatrix} &= \exp(j\varphi_+) \begin{bmatrix} j\sin\varphi_- & -j\cos\varphi_- \\ -j\cos\varphi_- & -j\sin\varphi_- \end{bmatrix} \begin{bmatrix} A_{n-1} \\ B_{n-1} \end{bmatrix} \\ &= \begin{bmatrix} j & 0 \\ 0 & 1 \end{bmatrix} \begin{bmatrix} \cos\left(\frac{\pi}{2}-\varphi_-\right) & -j\sin\left(\frac{\pi}{2}-\varphi_-\right) \\ -j\sin\left(\frac{\pi}{2}-\varphi_-\right) & \cos\left(\frac{\pi}{2}-\varphi_-\right) \end{bmatrix} \\ &\quad \times \begin{bmatrix} \exp(j\varphi_+) & 0 \\ 0 & -j\exp(j\varphi_+) \end{bmatrix} \begin{bmatrix} A_{n-1} \\ B_{n-1} \end{bmatrix} \end{aligned} \tag{13}$$

where

$$\varphi_+ = \frac{\varphi_u + \varphi_l}{2}, \quad \varphi_- = \frac{\varphi_u - \varphi_l}{2}. \tag{14}$$

As a result, Fig. 4(d) shows the modified unit-cell structure (nth unit-cell) with the following adjustments

$$\varphi'_{nr} = \varphi_6 + \frac{\pi}{2} + \varphi(2,3)_+ \tag{15}$$

$$\varphi'_{nt} = \varphi_1 - \frac{\pi}{2} + \varphi(2,3)_+ \tag{16}$$

$$\kappa'_{nr} = \frac{\pi}{2} - \varphi(2,3)_- \tag{17}$$

$$\kappa'_{nt} = \frac{\pi}{2} - \varphi(4,5)_- \tag{18}$$

where φ'_{nr} is the modified phase shift on the ring resonator, φ'_{nt} is the modified phase shift on the lower waveguide, κ'_{nr} is the modified coupling coefficient of the ring coupler, and κ'_{nt} is the modified coupling coefficient of the output coupler.

With the help of the modified unit-cell structure, we can still use the standard recursive algorithm [11] to find the optical parameters for each unit-cell. After that, we can recalculate the tuning value for each phase shifter. As a result, we can tune zeros for each unit cell with the recursive algorithm.

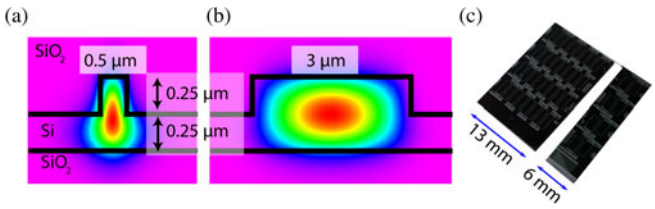

Fig. 5. Transverse electric (TE) mode profile for the (a) narrow and the (b) wide waveguides. (c) Photograph of the fabricated devices, containing a four unit-cell filter and a single unit-cell filter.

IV. Lattice Filter Implementation and Fabrication

The device implementation is on the silicon-on-insulator (SOI) platform. We choose to design the device using rib waveguides since they exhibit lower losses than channel waveguides and two widths of rib waveguides are used for the device design. Fig. 5(a) and (b) show the mode profile simulation for the 0.5-μm wide rib waveguide and the 3.0-μm wide rib waveguide, respectively [17]. The dimensions of the waveguides are a 500-nm core height, 250-nm rib height, 250-nm slab height, and 300-μm bending radius. The 3.0-μm waveguide has lower propagation loss due to lower photon density near the etched side walls and is primarily used as the ring resonator waveguide to achieve high Q-factor. We used 200-μm long parabolic tapers to adiabatically taper the 3.0-μm waveguides to 0.5-μm wide waveguides [10]. The narrower waveguides are primarily used for curved waveguide sections in the MZI and directional couplers to maintain the lowest order optical mode and in the phase shifter regions increase modulation efficiency.

The devices are fabricated in BAE Systems CMOS foundry and Microlab/Marvell Nanolab facilities, University of California, Berkeley. The fabrication process starts with a 6-in SOI wafer, which has a buried oxide layer of 3-μm thickness, and an upper silicon layer of 0.5-μm thickness [10]. The waveguide layer is defined using deep-ultraviolet (DUV) lithography stepper technology and incorporates photoresist reflow to obtain smooth waveguide sidewalls [18]. A transformer-coupled plasma reactive ion etching (TCP RIE) process, using a dielectric hard mask, forms the silicon rib waveguides. We use a second lithography process to create heat isolation trenches that reduce the thermal crosstalk between the tuning elements.

After the trenching process, we use dry thermal oxidation of silicon to reduce the waveguide sidewall corrugations. In order to obtain a 50/50 splitting ratio for the directional couplers, we optimized the fabrication process through several iterations to find the balance between the counteracting effects of the photoresist reflow, the waveguide oxidation and the waveguide etching depth. As a result, the final optimization produced a directional coupler with $<3\%$ splitting errors [10].

Boron and phosphorus ion implantations form the p- and n-doped regions. After the silicon oxide cladding deposition and planarization process, we densify the cladding and activate the implanted dopants in a common annealing step. Another sequence of lithographic definition and RIE process forms via openings through the cladding layer. The electrodes are comprised of sputtered aluminum film with a thin layer of

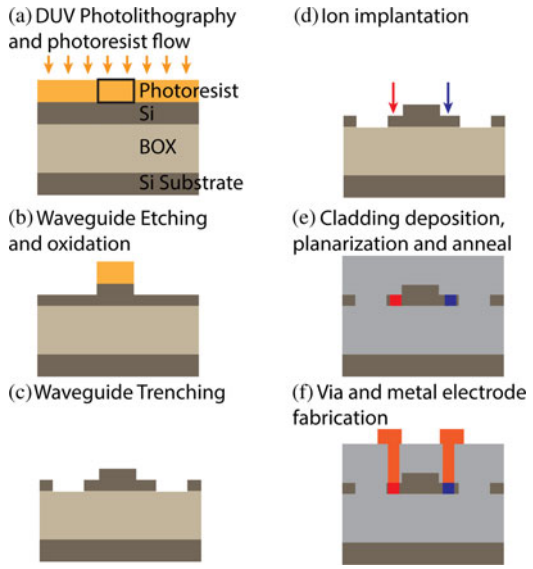

Fig. 6. Diagram of the fabrication process flow.

titanium/titanium nitride on top which is used as a protective barrier. Electrodes are patterned by lithographic definition and etched in Cl_2/BCl_3 plasma, followed by forming gas annealing to alloy the contacts and fill the domain wall traps in the sputtered metal. After the device singulation by diamond saw dicing, facet polishing allows the coupling of light to the fabricated devices. In addition, we add an anti-reflection coating to reduce coupling loss and the Fabry–Pérot effect. Fig. 6 shows the summary of the fabrication process flow.

V. Lattice Filter Characterization

As we discussed in Section III, both unit-cell and four-cell optical lattice filter reconfiguration requires filter synthesis. However, the actual tuning relies on the mapping the relationship between the induced optical phase shift and the injected electrical current. In this section, we describe the lattice filter characterization.

To fully characterize the devices we used an OVNA [19], [20] that employs polarization-sensitive, swept-wavelength interferometry to measure the transfer function of a device under test. There are several advantages of using an OVNA for lattice filter characterization, such as high optical spectral resolution (50 MHz), high dynamic range due to balanced detection and complex field measurement.

Fig. 7 shows the arrangement of the OVNA. The tunable laser operates as a swept wavelength source (up to 2000 nm/s) with a typical sweep range of 10 nm. The auxiliary interferometer (upper part of Fig. 7) is used to measure and correct for any nonlinearity in the frequency sweep of the laser.

The lower interferometer is used to measure the device under test (DUT). The data (signal output and auxiliary output) are acquired in the time domain using balanced detection followed by analog-to-digital conversion. Using digital signal processing in a PC, the Fourier transform of the acquired time domain signal provides the complex transfer function.

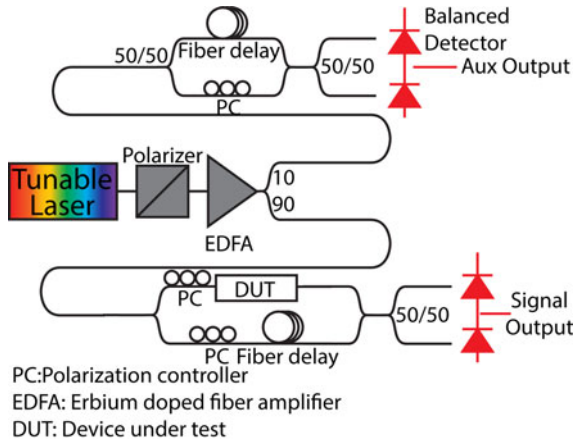

Fig. 7. Schematic of the OVNA.

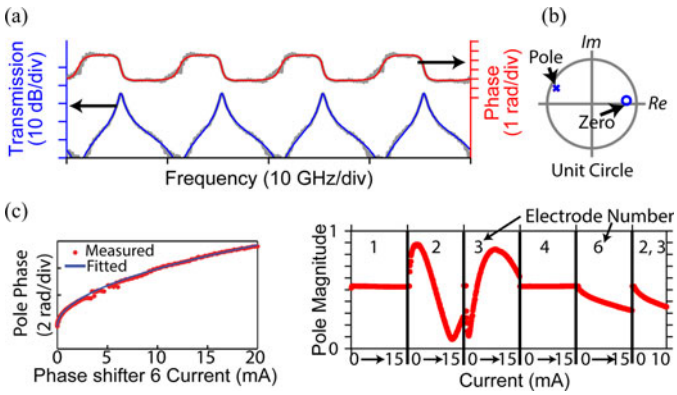

Fig. 8. (a) Unit-cell amplitude and phase measurement (grey) and waveform fitting (blue, red) for a 400-MHz 3-dB bandwidth bandpass filter. (b) Fitted pole and zero of the bandpass filter. (c) Optical parameter extraction with independent current sweeps of each phase shifter in Fig. 1(a).

The first step of characterization is to measure the basic device performance, such as waveguide loss, resonator Q-factor, and current injection induced optical loss. From our OVNA measurement results, the propagation loss for a 0.5-μm wide waveguide is 0.3 dB/cm. If we assume the excess loss limits the maximum of the pole magnitude, a worst-case estimation of the unit-cell round trip loss is 0.6 dB. The required current injection for 2π rad phase shift is 13 mA [13]. The Q-factor is 2.7×10^5 for a DUV fabricated device [10]. The induced loss for 2π rad phase tuning is 4 dB.

The second step of characterization is fitting to the measured transfer function. As we discussed in Section III, we use NEE as the filter fidelity metric. Fig. 8(a) shows an example of measured amplitude and phase (grey) and its corresponding fitted waveform (blue for magnitude, red for phase). The fitted waveform provides a numerical transfer function of the measured waveform. Therefore, we can extract the pole and zero from the transfer function. Fig. 8(b) shows the fitted result.

The third step is to characterize each optical parameter (such as the pole magnitude) by independently sweeping the current of each phase shifter. For a unit-cell structure, Fig. 8(c) shows the pole phase and magnitude when independently tuning the respective phase shifters. The left part of Fig. 8(c) shows the pole

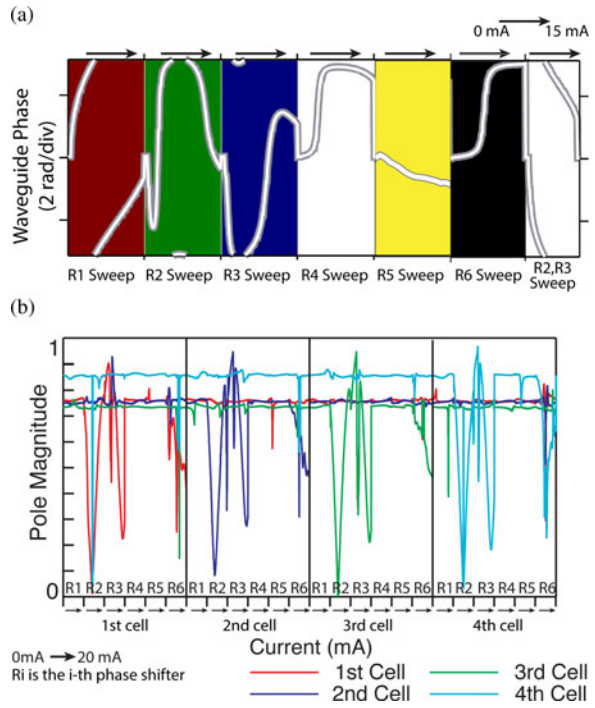

Fig. 9. Characterization result for (a) unit-cell lower waveguide phase with each phase shifter current sweeping, and (b) four-cell pole magnitude with each phase shifter current sweeping in the corresponding unit-cell.

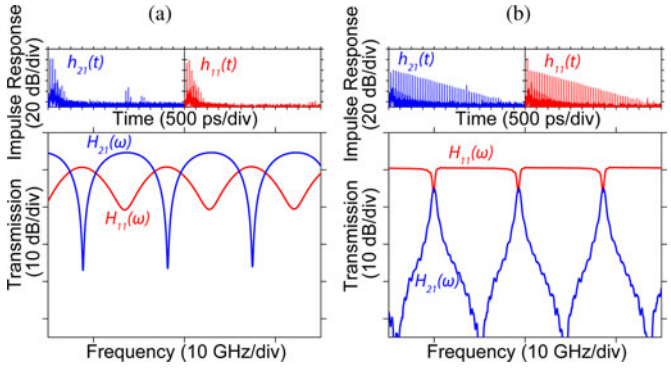

Fig. 10. Unit-cell optical filter with (a) weak resonance and (b) strong resonance. [13]. (a) Bandpass with small pole (FIR) pole magnitude = 0.11. (b) Bandpass with large pole (IIR) pole magnitude = 0.87.

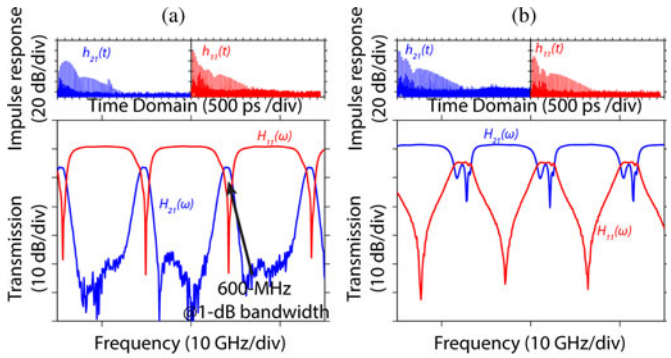

Fig. 11. Four-cell lattice filter tuning examples for (a) $H_{21}(\omega)$ with a -1-dB bandwidth of 600-MHz, -3-dB bandwidth of 1-GHz and -20-dB bandwidth of 2.8-GHz. (b) $H_{11}(\omega)$ with -1-dB bandwidth of 1.8-GHz, -3-dB bandwidth of 2.5-GHz and -20-dB bandwidth of 7.6 GHz. (a) Bandpass filter $H_{21}(\omega)$. (b) Notch filter $H_{21}(\omega)$.

phase tuning with ring phase shifter tuning [labeled as phase shifter 6 in Fig. 1(a)]. As expected, the pole is only affected by phase shifters 2, 3 and 6 as labeled in Fig. 1(a). In addition, the characterization result shows that the p-i-n diode phase changes proportionally to the square root of the injected current. This is expected from free carrier effect [14]. The tested threshold voltage of the p-i-n diode is 0.85 V.

For a four-cell structure, poles are independently controlled by each unit-cell, and zeros are coupled through the whole transfer function. Based on previous discussion in Section III, the recursive algorithm focuses on optical parameter tuning instead of zero tuning. Optical parameters are independently controlled by the unit-cells. Therefore, we can establish a mapping table between each of the optical parameters and corresponding injection currents [e.g., modified phase shift of the lower waveguide $\varphi_{nt}{}'$ in Fig. 4(d) links with phase shifter 1, 2 and 3 in Fig. 1(a)].

Fig. 9(a) shows that for a unit-cell structure, the lower waveguide phase is affected by phase shifters 1, 2, 3, 4, 5 and 6 in Fig. 1(a). Phase shifters 4, 5 and 6 can affect the lower waveguide phase mainly because of the heating effect. Fig. 9(b) shows that in a four-cell lattice filter, each pole can be affected by phase shifters 2, 3 and 6 in the unit-cell structure in Fig. 1(a). Here R_i ($i = 1,2,\ldots,6$) is defined as phase shifter of the unit-cell structure. The pole magnitude can be derived from the coupling coefficient of the ring coupler and waveguide loss. As expected, each pole is independently controlled by its own unit-cell structure.

Characterization results can help us build the look up table for each optical parameter and the different phase shifter injection currents. Therefore, it is necessary to perform the characterization for successful lattice filter reconfiguration.

VI. Experimental Results of a Reconfigurable Lattice Filter

In this section, we present both unit-cell and four-cell lattice filter reconfiguration examples. In addition, we also measured spurious free dynamic range (SFDR) of the unit-cell lattice filter, as well as the reconfiguration time between a bandpass filter and a notch filter for the unit-cell lattice filter.

Fig. 10(a), (b) shows the transfer function of $H_{11}(\omega)$ and $H_{21}(\omega)$ for a weak resonance (e.g., near FIR filter, pole magnitude is 0.11) case, and a strong resonance (e.g., IIR filter, pole magnitude is 0.87) case. As we discussed in Section III, the tuning procedure is: first, set pole magnitude and phase through the ring resonator phase shifter and the ring coupler phase shifters. Second, adjust the zero position with the lower waveguide phase shifter and the output coupler phase shifters [13].

Fig. 11 shows the transmission of the four-cell optical lattice filter tuning example. This filter requires adjustment of 26 phase shifters. Fig. 11(a) shows a narrow bandpass filter for $H_{21}(\omega)$ transmission [13]. The filter has more than 30-dB extinction ratio and its -1-dB bandwidth is 600-MHz. Fig. 11(b) shows a wider bandpass filter for $H_{11}(\omega)$ transmission, with -1-dB bandwidth of 1.8-GHz. In addition, Fig. 12 shows a four-cell optical lattice

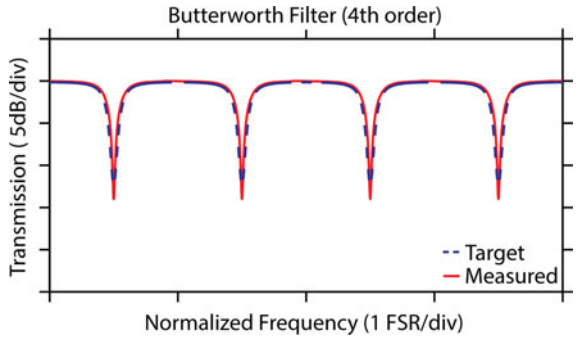

Fig. 12. Measured fourth-order Butterworth filter with 0.95 normalized cut-off frequency.

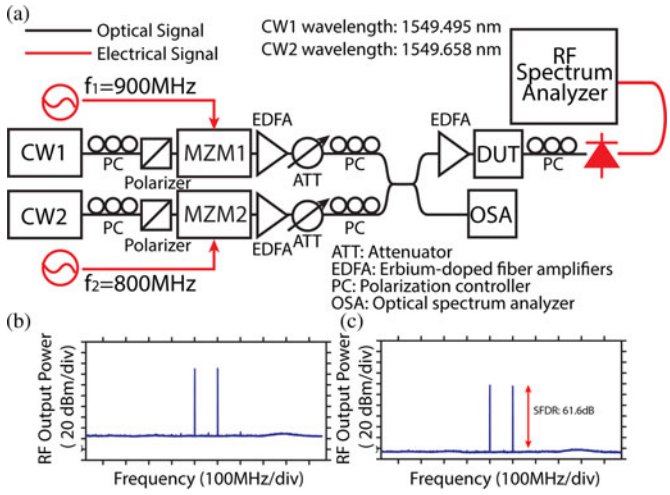

Fig. 13. (a) Experimental arrangement of the two-RF-tone SFDR measurement. Measured RF tones (b) before DUT (unit-cell) and (c) after DUT (unit-cell).

filter example of generating a fourth-order Butterworth filter with 0.95 normalized cut-off frequency. The filter reconfiguration follows the recursive algorithm discussed in Section III. As a result, we can conclude that the four-cell lattice filter (higher-order filter) can reconfigure for more complex and versatile filter shapes when compared to the unit-cell optical filter.

Next, we also performed a two-RF-tone SFDR measurement on a unit-cell reconfigurable filter. The two-RF-tones are used to modulate CW lasers and we measure the filtered output from the unit cell. Fig. 13(a) shows the experimental arrangement of the two-RF-tone measurement. We use two CW lasers as optical carriers at 1549.495 nm and 1549.658 nm, respectively. We separately modulate two MZIs, one at 800 MHz and other 900 MHz. The EDFAs and attenuators are used for equalizing the amplitudes of two RF tones before sending them to the unit-cell filter. We put an additional EDFA before the unit-cell to compensate for the 22-dB insertion loss of the device. The insertion loss was dominated by the coupling loss between the lensed fibers and 3.0-μm wide silicon waveguides at the polished optical facets. We estimate this coupling loss was 5–7 dB per facet. We monitor the wavelength with OSA on one output of the 2×2 directional coupler. On the other output, we use an Agilent 71400 C lightwave spectrum analyzer to detect the optical signal after the unit-cell filter and convert it to an electrical signal. The

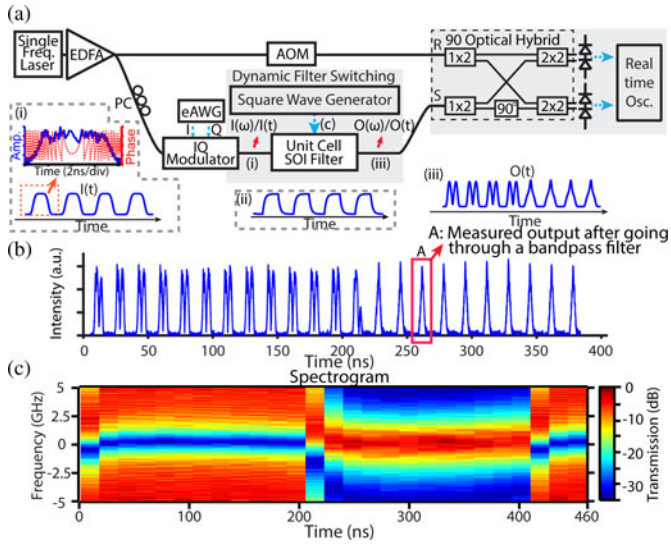

Fig. 14. (a) Experimental arrangement for measuring the dynamic reconfiguration of a unit-cell filter. (b)Measured waveform after the unit-cell filter with a 2.5-MHz switching speed. (c) 2D plot (spectrogram) showing the temporal evolution of the filter shape [21].

setup noise floor is -149 dBm/Hz. The measured SFDR is 61.6 dB. The total received optical power is -3.4 dBm. The resolution bandwidth of the RF spectrum analyzer is 30 kHz, the video bandwidth is 300 Hz. The sweep time is 116 s.

Finally, we also record the reconfiguration time of a unit-cell filter while switching from a bandpass filter to a notch filter. Fig. 14(a) shows the experimental arrangement for measuring the dynamic reconfiguration of a unit-cell optical filter [21]. We pass a train of linearly-chirped optical pulses through the unit cell filter. As a result, we can characterize the amplitude and phase of the pulses before and after the unit-cell filter. Fig. 14(b) shows the measured waveform intensities at the output of the unit-cell filter, when we applied a 2.5-MHz square waveform to lower waveguide phase shifter [labeled 1 in Fig. 1(a)]. A is the measured output waveform after going through a bandpass filter. Fig. 14(c) uses a spectrogram to present the dynamic reconfiguration between a notch filter and a bandpass filter. In conclusion, the major transition between two filter shapes is $<$16.67-ns. However, it might take 30–50 ns to fully stabilize the waveform after each transition, because of the device's thermal fluctuation with changing heat load (15–30 mW) [21].

VII. Applications

RF-photonic processing components have a broad range of applications due to their higher bandwidth, low latency performance, and potentially lower cost compared to all-electronic processing. This section focuses on using RF-photonic lattice filters to replace electrical signal processing in THz waveform synthesis.

One of the challenges in THz waveform synthesis is correcting the non-ideal frequency response of optical modulators and multiplexers. For example, Fig. 15(a) shows the general methodology for a dynamic optical arbitrary waveform generation (OAWG) transmitter, which is capable of generating arbitrary optical waveforms [e.g., Fig. 15(b)] within its operation

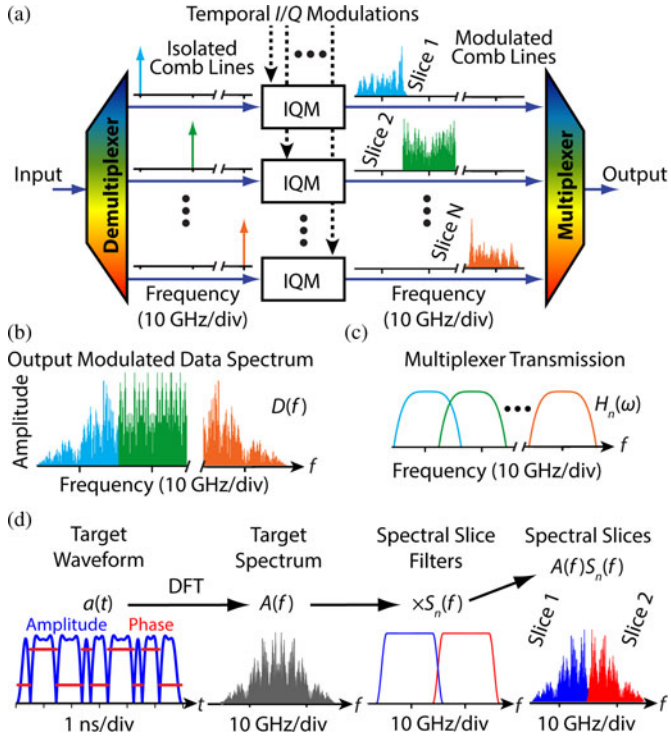

Fig. 15. (a) Dynamic OAWG transmitter diagram. (b) An example of output modulated data spectrum. (c) Multiplexer transfer function. (d) Signal processing for derive modulation signals. [12]

bandwidth. OAWG functions by first spectrally demultiplexing an optical frequency comb (OFC) to isolate each comb line on a separate output. In parallel, each comb line is then individually modulated using separate in-phase and quadrature-phase modulators. These modulated comb lines are then spectrally combined using a multiplexer with overlapping spectral passbands [Fig. 15(c)] to yield an arbitrary waveform that has a total bandwidth of $B\times N$, where B is the OFC line spacing and N is the number of OFC lines. In practice, a B of 10 GHz is a good compromise for both the electrical and optical components necessary for OAWG [22]. Of course, it is also possible to use a passive combiner instead of a spectral multiplexer to combine the modulated OFC lines, but this method is not practically scalable to large numbers of OFC lines due to increased optical losses.

The modulations necessary to broaden each OFC line can be derived according to Fig. 15(d). The first step is to determine a desired target waveform with bandwidth $B\times N$. Next, applying spectral slice filters to the Fourier transform of the target waveform yields spectral slices that are of manageable bandwidth for both electronic and optics (e.g., 10 GHz). Note that the spectral slice filters are a mathematical construct that serve only to divide the target waveform spectrum into spectral slices and do not result in any loss of information. Taking the inverse Fourier transform of each spectral slice yields the in-phase and quadrature-phase modulations necessary to drive each *I/Q* modulator for the generation of the target waveform at the output of the spectral multiplexer.

Experimental demonstrations of OAWG have relied on electronic precompensation to compensate for the non-ideal frequency response of the *I/Q* modulators and the transmission

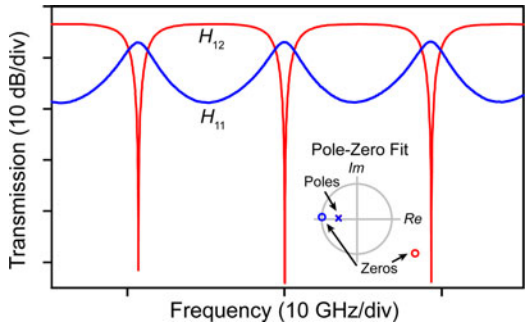

Fig. 16. Measured transmission of a unit-cell filter as an optical equalizer of $H_{11}(f)$ ($H_{12}(f)$ is the complementary output). Fitted pole and zeros are presented in the part of the plot [12].

function of the spectral multiplexer [22]. Relying solely on electronic compensation, however, reduces the effective dynamic range available for OFC line modulation while increasing complexity and power consumption of the electronics.

Reconfigurable RF-photonic lattice filters [10] are a viable optical solution for overcoming both the non-ideal *I/Q* modulator response and the spectral multiplexer transmission in THz waveform synthesis. In this case, a 10-GHz FSR unit-cell filter can function as an optical equalization component for an OAWG waveform created using 10 GHz spectral slices. Specifically, the unit-cell based filter can be placed immediately after the output of the OAWG transmitter. Fig. 16 shows the measured transmission of a unit-cell filter [$H_{11}(f)$ as output] when configured as an optical equalizer for OAWG. The inset in Fig. 16 shows the corresponding pole and zeros position for the unit-cell filter [zeros are from $H_{11}(f)$ and $H_{12}(f)$]. The unit-cell optical filter provides nearly identical equalization to that which can be achieved using a digital filter. Moreover, using optical processing, instead of digital processing, reduces the complexity of the required electrical components, and reduces power consumption.

Further investigations evaluated OAWG waveform Q-factor as a function of digital-to-analog converter (DAC) effective number of bits (ENOB) using electrical equalization or optical equalization via simulations [12]. The target waveform consisted of a 5-ns, 100-Gb/s BPSK signal (500 bits) with a signal to noise ratio of 15 dB. The resulting 100-GHz signal waveform was divided into ten 10-GHz spectral slices following the methodology in Fig. 15(d). The electrical equalization scenario involved the application of pre-emphasis on the modulator driven signal to correct for the non-ideal frequency response of the *I/Q* modulators and the spectral multiplexer. The optical equalization scenario consisted of using a reconfigurable unit-cell lattice filter to provide the necessary compensation. After applying equalization, calculation of the waveform Q-factor from the simulated constellation enabled evaluating the efficacy of both methods of compensation. Fig. 17 shows the simulated Q-factor as a function of DAC ENOB for both optical equalization and electrical equalization. Optical equalization shows higher Q-factor at all DAC ENOB values, which indicates improved waveform fidelity. Electrical equalization had reduced performance due to a reduction in DAC ENOB available for *I/Q* modulator modulations after accounting for the necessary

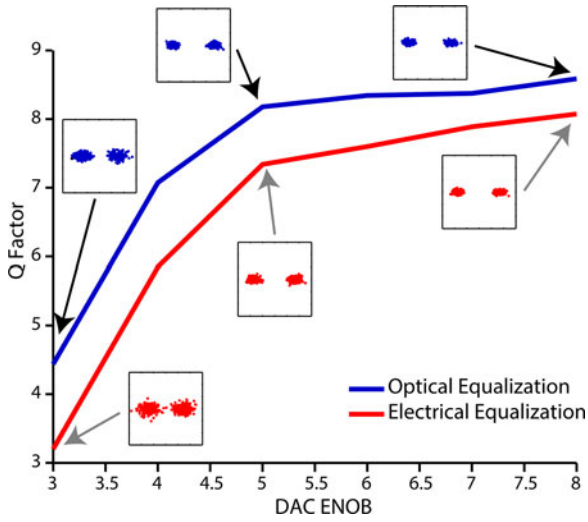

Fig. 17. Simulated Q-factor with DAC ENOB for both optical equalization and electrical equalization. Simulation uses 10, 10-GHz spectral slice to generate data waveforms in the BPSK modulation format [12].

compensation. As a result, optical equalization shows improved performance compared to electrical equalization for the same DAC ENOB.

VIII. Conclusion

This paper presented unit-cell and four-cell silicon CMOS compatible lattice filters suitable for RF signal processing. Exploiting the benefits of optical processing components in RF photonics can provide low-cost and low latency signal processing. A theoretical lattice filter analysis combined with a recursive lattice filter reconfiguration algorithm, provided a detailed solution for implemented arbitrary and complex lattice filter configurations. Lattice filters enable reconfiguration of filter shape in the RF domain (10-GHz FSR), with low induced loss (4 dB per 2π shift), sub-20-ns reconfiguration time, and fully independent control of the filter's poles and zeros. The characterization results built up useful look-up table for reconfiguration. In addition, the experimental results proved that the lattice filter successfully generated narrow bandwidth bandpass filters and notch filters, as well as a complex filter shape (fourth order Butterworth filter). The high SFDR (61.5 dB) achieved also indicates high linear performance of the silicon photonic devices. Applications of optical lattice filters to optical signal processing enables replacing electrical signal processing components. Future developments with higher order optical lattice filters can further improve the achievable gain compensation and improve the reconfiguration performance.

References

[1] E. M. Dowling and D. L. MacFarlane, "Lightwave lattice filters for optically multiplexed communication systems," *J. Lightw. Technol.*, vol. 12, no. 3, pp. 471–486, Mar. 1994.

[2] J. Capmany, B. Ortega, and D. Pastor, "A tutorial on microwave photonic filters," *J. Lightw. Technol.*, vol. 24, no. 1, pp. 201–229, Jan. 2006.

[3] K. Okamoto, K. Takiguchi, and Y. Ohmori, "16-channel optical add/drop multiplexer using silica-based arrayed-waveguide gratings," *Electron. Lett.*, vol. 31, pp. 723–724, 1995.

[4] Q. Xu and M. Lipson, "All-optical logic based on silicon micro-ring resonators," *Opt. Exp.*, vol. 15, pp. 924–929, 2007.

[5] M. S. Rasras, D. M. Gill, M. P. Earnshaw, C. R. Doerr, J. S. Weiner, C. A. Bolle, and Y.-K. Chen, "CMOS silicon receiver integrated with Ge detector and reconfigurable optical filter," *IEEE Photon. Technol. Lett.*, vol. 22, no. 2, pp. 112–114, Jan. 2010.

[6] M. S. Dahlem, C. W. Holzwarth, A. Khilo, F. X. Kartner, H. I. Smith, and E. P. Ippen, "Reconfigurable multi-channel second-order silicon microring-resonator filterbanks for on-chip WDM systems," in *Proc. Photon. Global Conf.*, 2010, pp. 1–3.

[7] E. J. Norberg, R. S. Guzzon, S. C. Nicholes, J. S. Parker, and L. A. Coldren, "Programmable photonic lattice filters in InGaAsP–InP," *IEEE Photon. Technol. Lett.*, vol. 22, no. 2, pp. 109–111, Jan. 2010.

[8] P. Alipour, A. A. Eftekhar, A. H. Atabaki, Q. Li, S. Yegnanarayanan, C. K. Madsen, and A. Adibi, "Fully reconfigurable compact RF photonic filters using high-Q silicon microdisk resonators," in *Proc. Opt. Fiber Commun. Conf.*, 2011, pp. 1–2, Paper OThM5.

[9] P. Dong, N.-N. Feng, D. Feng, W. Qian, H. Liang, D. C. Lee, B. J. Luff, T. Banwell, A. Agarwal, P. Toliver, R. Menendez, T. K. Woodward, and M. Asghari, "GHz-bandwidth optical filters based on high-order silicon ring resonators," *Opt. Exp.*, vol. 18, pp. 23784–23789, 2010.

[10] S. Ibrahim, N. K. Fontaine, S. S. Djordjevic, B. Guan, T. Su, S. Cheung, R. P. Scott, A. T. Pomerene, L. L. Seaford, C. M. Hill, S. Danziger, Z. Ding, K. Okamoto, and S. J. B. Yoo, "Demonstration of a fast-reconfigurable silicon CMOS optical lattice filter," *Opt. Exp.*, vol. 19, pp. 13245–13256, 2011.

[11] K. Jinguji, "Synthesis of coherent two-port optical delay-line circuit with ring waveguides," *J. Lightw. Technol.*, vol. 14, no. 8, pp. 1882–1898, Aug. 1996.

[12] S. J. B. Yoo, R. P. Scott, D. J. Geisler, N. K. Fontaine, and F. M. Soares, "Terahertz information and signal processing by RF-photonics," *IEEE Trans. THz Sci. Technol.*, vol. 2, no. 2, pp. 167–176, Mar. 2012.

[13] N. K. Fontaine, S. Ibrahim, S. S. Djordjevic, B. Guan, T. Su, S. Cheung, R. Yu, R. P. Scott, A. T. Pomerene, L. L. Seaford, C. M. Hill, S. Danziger, Z. Ding, K. Okamoto, and S. J. B. Yoo, "Fully reconfigurable silicon CMOS photonic lattice filters," in *Proc. 36th Eur. Conf. Exhib. Opt. Commun.*, 2010, pp. 1–3, Paper Tu.4.C.3.

[14] R. A. Soref and B. R. Bennett, "Electrooptical effects in silicon," *IEEE J. Quantum Electron.*, vol. 23, no. 1, pp. 123–129, Jan. 1987.

[15] R. P. Scott, N. K. Fontaine, J. P. Heritage, and S. Yoo, "Dynamic optical arbitrary waveform generation and measurement," *Opt. Exp.*, vol. 18, pp. 18655–18670, 2010.

[16] C. K. Madsen and J. H. Zhao, *Optical Filter Design and Analysis: A Signal Processing Approach*. New York: Wiley, 2001.

[17] L. Zhou, S. Djordjevic, N. K. Fontaine, Z. Ding, K. Okamoto, and S. J. B. Yoo, "Silicon microring resonator-based reconfigurable optical lattice filter for on-chip optical signal processing," in *Proc. IEEE LEOS Annu. Meeting Conf. Proc.*, 2009, pp. 501–502.

[18] S. T. S. Cheung, B. Guan, S. S. Djordjevic, K. Okamoto, and S. J. B. Yoo, "Low-loss and high contrast silicon-on-insulator (SOI) arrayed waveguide grating," in *Proc. Conf. Lasers Electro-Opt.*, 2012, pp. 1–2.

[19] D. K. Gifford, B. J. Soller, M. S. Wolfe, and M. E. Froggatt, "Optical vector network analyzer for single-scan measurements of loss, group delay, and polarization mode dispersion," *Appl. Opt.*, vol. 44, pp. 7282–7286, 2005.

[20] G. D. VanWiggeren and D. M. Baney, "Swept-wavelength interferometric analysis of multiport components," *IEEE Photon. Technol. Lett.*, vol. 15, pp. 1267–1269, 2003.

[21] B. Guan, N. K. Fontaine, S. S. Djordjevic, S. Cheung, R. P. Scott, D. J. Geisler, and S. J. B. Yoo, "Full-field technique for measuring the spectral evolution of reconfigurable photonic filters," *Opt. Lett.*, vol. 37, pp. 341–343, 2012.

[22] D. J. Geisler, N. K. Fontaine, R. P. Scott, T. He, L. Paraschis, O. Gerstel, J. P. Heritage, and S. J. B. Yoo, "Bandwidth scalable, coherent transmitter based on the parallel synthesis of multiple spectral slices using optical arbitrary waveform generation," *Opt. Exp.*, vol. 19, pp. 8242–8253, 2011.

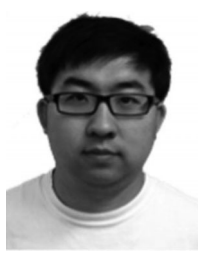

Binbin Guan received the B.S. degree in optics engineering from Zhejiang University, China, in 2008. He is currently working toward the Ph.D. degree in electrical and computer engineering at the University of California, Davis, CA, USA. His current graduate research focuses on optical coherent communications and optical signal processing.

Stevan S. Djordjevic received the Dipl.-Ing. degree from the School of Electrical Engineering, University of Belgrade, Serbia. He is currently working toward the Ph.D. degree in electrical and computer engineering at the University of California, Davis, CA, USA. During his graduate research, he has designed, fabricated, and characterized CMOS-compatible athermal silicon ring modulators, reconfigurable silicon photonic lattice filters, and other integrated optical devices. He is currently with the Photonics, Interconnects, and Packaging Group, Oracle Labs, San Diego, CA, working on the DARPA Ultra-performance Nanophotonic Intrachip Communication (UNIC) project.

Nicolas K. Fontaine (S'02–M'10) received B.S. degrees in both electrical engineering and optical engineering , the M.S. degree in electrical and computer engineering,and the Ph.D. degree in electrical and computer engineering from from the University of California (UC), Davis, CA, USA, in 2004, 2007, and 2010, respectively. He is currently a Member of Technical Staff at Bell Laboratories, Alcatel-Lucent, Holmdel, NJ, USA.

Linjie Zhou, photograph and biography not available at the time of publication.

Salah Ibrahim received the B.Sc. and M.Sc. degrees in electronics and communication engineering from Cairo University, Egypt, and the Ph.D. degree in electronics engineering from the University of Tokyo, Japan, in 2009. From 2009 to 2010, he was a Postdoctoral Research Scientist in the Department of Electrical and Computer Engineering, University of California, Davis, CA, USA. Since 2011, he is with NTT Photonics Laboratories, Atsugi, Japan. His current research interests include OPS technologies, ultrafast optoelectronic and optical device in InP, silicon and hybrid material systems.

Ryan P. Scott (S'93–M'03) received the B.S. degree in laser electrooptics technology from the Oregon Institute of Technology, Klamath Falls, in 1991, the M.S. degree in electrical engineering from the University of California, Los Angeles, in 1995, and the Ph.D. degree in electrical and computer engineering from the University of California, Davis (UC Davis), CA, USA, in 2009. He is currently a Project Scientist in the Department of Electrical and Computer Engineering, UC Davis. His current research interests include photonic integration of complex optical systems to improve stability and expand applications, full-field optical waveform generation and measurement techniques, and spatial division multiplexing technologies.

David J. Geisler (S'02–M'12) was born in New York, NY, USA, in 1982. He received the B.S. degree in electrical engineering from Tufts University, Medford, MA, USA, in 2004, the M.S. degree in electrical engineering from the University of California, Davis, CA, USA, in 2009, and the Ph.D. degree in electrical and computer engineering from the University of California, Davis, in 2012.

He is currently with the Advanced Lasercom and Systems Group, Massachusetts Institute of Technology Lincoln Laboratory, Lexington, MA, USA. His research interests include optical arbitrary waveform generation and measurement, advanced modulation formats, and free-space optical communications.

Zhi Ding (S'88–M'90–SM'95–F'03) received the Ph.D. degree in electrical engineering from Cornell University in 1990. He is the Child Family Endowed Professor of Engineering and Entrepreneurship at the University of California, Davis, CA, USA. He also holds a joint appointment as a thousand talent professorship at Southeast University in Nanjing, China From 1990 to 2000, he was a Faculty Member of Auburn University and later, University of Iowa. He has held visiting positions in Australian National University, Hong Kong University of Science and Technology, NASA Lewis Research Center and USAF Wright Laboratory. He has active collaboration with researchers from several countries including Australia, China, Japan, Canada, Taiwan, Korea, Singapore, and Hong Kong. He has been an active member of IEEE, serving on technical programs of several workshops and conferences. He was an Associate Editor for IEEE TRANSACTIONS ON SIGNAL PROCESSING from 1994 to 1997, 2001 to 2004, and an Associate Editor of IEEE SIGNAL PROCESSING LETTERS 2002–2005. He was a member of technical committee on Statistical Signal and Array Processing and member of technical committee on Signal Processing for Communications (1994–2003). He was the Technical Program Chair of the 2006 IEEE Globecom. He is also an IEEE Distinguished Lecturer (Circuits and Systems Society, 2004–06, Communications Society, 2008–09). He served as an IEEE TRANSACTIONS ON WIRELESS COMMUNICATIONS Steering Committee Member (2007–2009) and its Chair (2009–2010). He is a coauthor of the book *Modern Digital and Analog Communication Systems*, (4th edition, Oxford University Press, 2009).

S. J. Ben Yoo (S'82–M'84– SM'97–F'07) received the B.S. degree in electrical engineering (with distinction), the M.S. degree in electrical engineering, and the Ph.D. degree in electrical engineering with minor in physics, all from Stanford University, Stanford, CA, USA, in 1984, 1986, and 1991, respectively. He currently serves as Professor of electrical engineering at the University of California at Davis (UC Davis). His research at UC Davis includes RF-photonic devices, systems, and networking technologies for the future generation Internet and computing systems. In particular, he is conducting research on architectures, systems integration, and network experiments related to all-optical label switching routers, terahertz optical arbitrary waveform generation, flexible bandwidth networking, and optical interconnect technologies. Prior to joining UC Davis in 1999, he was a Senior Research Scientist at Bell Communications Research (Bellcore), leading technical efforts in optical networking research and systems integration. His research interests at Bellcore included optical-label switching for the next-generation Internet, power transients in reconfigurable optical networks, wavelength interchanging cross connects, wavelength converters, vertical-cavity lasers, and high-speed modulators. He also participated in the advanced technology demonstration network/multiwavelength optical networking (ATD/MONET) systems integration, the OC-192 synchronous optical network (SONET) ring studies, and a number of standardization activities which led to documentations of Generic Requirements, GR-2918-CORE (1999), GR-2918-ILR (1999), GR-1377-CORE (1995), and GR-1377-ILR (1995) on dense WDM and OC-192 systems. Prior to joining Bellcore in 1991, he conducted research at Stanford University on nonlinear optical processes in quantum wells, a four-wave-mixing study of relaxation mechanisms, and ultrafast diffusion-driven photodetectors. During this period, he also conducted research on lifetime measurements of intersubband transitions and on nonlinear optical storage mechanisms at Bell Laboratories and IBM Research Laboratories, respectively. Dr. Yoo is a Fellow of IEEE Photonics Society, a Fellow of the Optical Society of America (OSA), a Fellow of NASA NIAC, and a Member of Tau Beta Pi. He received the DARPA Award for Sustained Excellence in 1997, the Bellcore CEO Award in 1998, the Outstanding Mid-Career Research Faculty Award (UC Davis) in 2004, and the Outstanding Senior Research Faculty Award (UC Davis) in 2011. He also served as an Associate Editor for IEEE PHOTONICS TECHNOLOGY LETTERS, Guest Editor for IEEE/OSA JOURNAL OF LIGHTWAVE TECHNOLOGY and IEEE JOURNAL OF SELECTED TOPICS IN QUANTUM ELECTRONICS, and General Cochair for Photonics in Switching conference 2007, 2010, and 2012.